Wormlike Micellar Solutions: III. VCM Model Predictions in Steady and Transient Shearing Flows

Lin Zhou,[a] Gareth H. McKinley,[b] L.Pamela Cook[c]

[a]*Department of Mathematics, New York City College of Technology, Brooklyn, NY,*
11201

[b]*Department of Mechanical Engineering, Massachusetts Institute of Technology,*
Cambridge, MA. 02139

[c]*Department of Mathematical Sciences, University of Delaware, Newark, DE.*
19716

Abstract

The two species, scission/reforming Vasquez-Cook-McKinley (VCM) model was formulated to describe the coupling between the viscoelastic fluid rheology and the kinetics of wormlike micellar assembly and deformation-induced rupture. The model self-consistently captures the nonlocal effects of stress-induced diffusion and has been studied in various limits for a number of canonical flow fields including Large Amplitude Oscillatory Shear (LAOS), steady and transient extensional flow as well as steady pressure-driven channel flow. However, a complete study of the spatiotemporal model predictions, both with (and without) inertia, and with (or without) the stress-concentration diffusive coupling, has not yet been reported. In this paper we present a comprehensive investigation of the full VCM model in steady and transient shearing flow including inertial and diffusive (non-local) effects. The consequences

of varying the model parameters, the effect of the start-up ramp rate, and the role of geometry on the steady state flow curve are each investigated. As a result of the onset of shear-banding and nonlocal effects in the velocity, stress and concentration profiles, we show that the measured rheological properties in a wormlike micellar solution described by the VCM model can depend on the initial ramp rate as well as specific details of the geometry such as the length scale of the rheometric fixture chosen and its curvature. The complete time evolution of the rheological response at high Deborah numbers is examined, from the initial formation of inertial waves through nonlinear overshoots in the viscoelastic stresses, shear band formation (and elastic recoil in the local velocity), to the long time diffusion-mediated approach to a final steady state.

Key words: VCM model, shear banding, wormlike micelles

1 Introduction

Wormlike micellar mixtures exhibit properties making them valuable for commercial uses, for example in detergents, shampoos and as oil recovery enhancers. These mixtures show high and constant viscosities at low shear rates with strong shear thinning occurring at larger shear rates. Wormlike micelles are composed of amphiphilic surfactant amphiphilic molecules which, in an aqueous solvent, self assemble into long flexible cylindrical (wormy) structures protecting their hydrophobic tails in the interior of the worm. The length of the worms can be on the order of microns with radii on the order of tens of nanometers. These long flexible worms entangle in solution at moderate

Email addresses: `LZhou@CityTech.Cuny.edu` (Lin Zhou,), `gareth@mit.edu` (Gareth H. McKinley,), `cook@math.udel.edu` (L.Pamela Cook).

surfactant concentrations and, as a result of these entanglements, wormlike surfactant mixtures exhibit visco-elastic properties similar to those exhibited by concentrated polymer solutions. By contrast with covalently-connected flexible polymer chains, the wormlike micelles continuously break and reform thus earning the name 'living polymers'. The rheology of these mixtures is dominated by two distinct relaxation processes; firstly a disentanglement process in which the worms dissociate from the network, similar to reptation of entangled polymers, the second due to the breakage and reformation of the worms.

Wormlike micellar solutions of various chemistries (CPyCl, CTAB, EHAC) in a range of solvents have been the subject of many experimental investigations, for example [1, 2, 3, 4, 5, 6, 7]. A good overview of experimental findings and the surfactants used in each is given in [8]. These experiments show a commonality in the rheological response of these mixtures in that they can exhibit kinematic inhomogeneities even in simple shearing flow, developing shear-bands and strong shear-thinning. In a narrow gap Taylor-Couette device, with inner cylinder rotating at a fixed velocity and outer cylinder fixed, the steady state velocity profile across the gap is nearly linear at low shear rates. When the velocity of the inner cylinder is increased such that the velocity gradient across the gap exceeds a critical shear rate, $\dot{\gamma}_1$, the velocity profile splits into (at least) two regions; with a high shear rate (i.e. large velocity gradient) near the inner wall and a slower moving region with low shear rate closer to the outer wall. The transition region between the two shear bands shifts outwards toward the stationary outer cylinder as the shear rate is increased until, at a certain shear rate, $\dot{\gamma}_2$, the high shear rate band spans the gap. At shear rates larger than $\dot{\gamma}_2$, the velocity profile is again close to linear. The steady state flow curve of shear stress as a function of shear rate rises monotonically

(almost linear) for small shear rates, then begins to level off until, at the shear rate of $\dot{\gamma}_1$ the flow curve plateaus. The plateau continues until the shear rate reaches $\dot{\gamma}_2$, thereafter the flow curve is again a monotonic increasing function of shear rate. Experiments also show [7] that under shear rate control the first normal stress difference initially increases quadratically with shear rate until $\dot{\gamma}_1$, at which point the increase becomes linear, up to a shear rate of $\dot{\gamma}_2$, at which point the rate of increase in N_1 becomes approximately quadratic again. Small Amplitude Oscillatory Shear (SAOS) experiments show two highly separated time scales suggesting a superposition of two Maxwell modes [7]. The shear-banding, and the correlated flow curve plateau, are generally attributed to a multi-valued underlying rheological constitutive relation between shear stress and shear rate if one assumes viscometric (homogeneous) kinematics [8, 9, 10]. Flows along the locally decreasing portion of this rheological constitutive curve have been shown to be unstable [11] so that, under shear-rate controlled conditions (with velocity imposed at the walls) the flow bifurcates into two branches with one flow domain located on the stable low shear rate branch of the rheological flow curve and the other on the stable high shear rate branch. The portion of the gap which each shear rate occupies is determined by a lever rule in order that the appropriate total velocity change across the gap is obtained. A number of comprehensive review papers describing the flow structure and dynamics have appeared [8, 9, 10].

Several single species (plus solvent) models which exhibit non-monotone rheological constitutive curves have been examined in the literature as a basis for understanding flows of wormlike micellar solutions; for example, the Johnson-Segalman model [12, 13, 14, 15], the reptation-reaction model [10, 16], a "Toy" model based on reptation theory [17], a more complete reptation model (known

as the "Rolie-Poly" model) [18], the Giesekus model [19, 20, 21] and the PEC (Partially Extended Convection) model [22]. These models can, under appropriate parameter conditions, all exhibit a non-monotone rheological constitutive curve and thus can each capture key aspects of the linear and nonlinear rheology observed experimentally. Some of these single-species models are phenomenological in basis (e.g. the Johnson-Segalman and Giesekus model) and may respond unphysically in step-strain and/or extensional flow response (e.g. the Johnson-Segalman model [23]), or may be difficult to manipulate and fit to actual experimental data (the reptation-reaction model). These single species models generally coarse-grain the solvent and low molecular weight species into a single Newtonian mode and thus do not exhibit fluid elasticity at high frequencies or shear rates.

One model that takes into account (in an approximate way) the breakage and reforming of the worms is the Vasquez-Cook-McKinley (VCM) model [24]. This model is a two species (plus solvent) model in which worms of length L can break into two worms of length $L/2$, and two worms of length $L/2$ can reform to a single worm of length L. The VCM model thus incorporates a physical breakage-reforming processes and is appropriately frame-invariant. The model allows for a realistic (aqueous) solvent viscosity and also captures the presence of a second, short species which gives rise to a weak viscoelastic contribution at high shear rates. The VCM model reduces to a single species PEC model (with additional diffusive terms) [23] in a Newtonian solvent, in the limit that the relaxation time of the second species goes to zero and that the number densities of each wormy species are constant. The PEC model was extensively examined in [22]. The Rolie-Poly model, in the limit that the convective constraint parameter β is zero and chain stretching is ignored, can

also be reduced to the reptation-reaction model [25]. In shearing flow, in that same limit, the Rolie-Poly model is similar to the PEC model but without the free nonlinear parameter. More recently, a thermodynamically consistent two-species model has been derived from non-equilibrium thermodynamics considerations and its predictions have been compared with those of the two-species VCM model [26].

Analysis of the rheological predictions of the VCM model has been carried out in several geometries and for a range of boundary conditions including steady shearing-flow in a Taylor-Couette geometry under Large Amplitude Oscillatory Shear (LAOS) [27]; fast and slow stepped-ramps up to steady state shearing in a Taylor-Couette geometry (during which localized shear waves may develop) [28]; steady pressure-driven channel flows [29], and extensional flows [30]. Predictions of those studies compare well with many of the principal features of wormlike micellar rheology observed in experiments. In these previous studies, theoretical predictions are contrasted with those of simpler single species models and shown to be an improvement in several cases, for example the capability of predicting the highly localized rupture event in an elongating filament of a wormlike micellar solution in extensional flow [30]. The predictions of a non-interacting version of the two species VCM model, namely the PEC+M model (as well as the PEC model plus solvent) have been analyzed extensively for the case of step strains and ramps up to steady state shearing flows [22].

While the VCM model has been demonstrated to successfully model wormlike micellar mixtures in various shearing and elongational deformations, it does have its own limitations including: (i) the second normal stress difference N_2 is identically zero; (ii) numerical simulations of steady state values of N_1, the

6

first normal stress difference, as a function of shear rate in *Taylor-Couette* flow do not agree with results obtained in *cone-plate* experiments for shear rates in the shear banding region [7]. This latter discrepancy may be due to the geometrical differences, but may also be due to the simplicity of the kinetics describing the reforming rate of the VCM model, a simplification made in part to highlight the controlling role of micellar breakage in the observed dynamics. In [31], the VCM model was modified, allowing temporal and configuration dependent changes of the equilibrium breakage rate and of the relaxation rate of the long species in order to account for gel-like structure formation that can be observed in some micellar solutions at very high deformation rates [32, 33].

As noted above, building on the VCM model success, a thermodynamically consistent two species model has recently been derived [26]. In this new model the nonlinear breakage and reforming rates have different functional forms than those of the VCM model. Preliminary simulations of the modified model in a homogeneous viscometric flow showed a multi-valued underlying rheological constitutive relation (flow curve), and a homogenous extensional flow curve similar to those of the VCM model. Results for inhomogeneous flows of this new model have not yet been reported. One advantage of the new model is that there is no free nonlinear parameter, on the other hand this distinction may well restrict the ability of the model to be fitted to experimental data for different micellar concentration.

In the present paper we carry out a comprehensive investigation of the full VCM model in shearing deformations including transient analysis from initial start up to steady state for a Taylor-Couette flow geometry. We compile a number of disparate existing results describing the VCM model predictions, and also provide new computational results; for example the effect of chang-

7

ing flow geometry on the steady state curve together with an experimental comparison. The full VCM model includes the effect of fluid inertia and the role of diffusive (nonlocal) terms which couple the local distribution in number density of each species, local stress gradients and the sharp variations in the local velocity within the shear bands. We also examine the full temporal responses of the system of the equation from short time (elastic waves) to long time (slow diffusive relaxation).

2 The Model Formulation

The detailed derivation of the VCM model can be found in [24]. In summary, the (non-dimensional) number density and stress equations are given by:

$$\mu \frac{Dn_A}{Dt} = 2\delta_A \nabla^2 n_A - \delta_A \nabla\nabla : \mathbf{A} + \frac{1}{2} c_B n_B^2 - c_A n_A, \tag{1a}$$

$$\mu \frac{Dn_B}{Dt} = 2\delta_B \nabla^2 n_B - 2\delta_B \ \nabla\nabla : \mathbf{B} - c_B n_B^2 + 2c_A n_A, \tag{1b}$$

$$\mu \mathbf{A}_{(1)} + \mathbf{A} - n_A \mathbf{I} - \delta_A \nabla^2 \mathbf{A} = c_B \, n_B \, \mathbf{B} - c_A \mathbf{A}, \tag{2a}$$

$$\epsilon\mu \mathbf{B}_{(1)} + \mathbf{B} - \frac{n_B}{2} \mathbf{I} - \epsilon\delta_B \nabla^2 \mathbf{B} = -2\epsilon \, c_B \, n_B \, \mathbf{B} + 2\epsilon \, c_A \mathbf{A}, \tag{2b}$$

where the breakage rate varies with the local shear rate according to $c_A = c_{Aeq} + \frac{\xi\mu}{3}(\dot{\boldsymbol{\gamma}} : \mathbf{A}/n_A)$, and for simplicity the reforming rate is taken to be constant, $c_B = c_{Beq}$. Here c_{Aeq} and c_{Beq} are the equilibrium breakage and reforming rates, respectively. The parameter $\mu = \lambda_A/\lambda_{eff} = 1 + c_{Aeq}$ measures the ratio of the stress relaxation time of the long species (denoted A) to the effective relaxation time of the total network. Since micellar breakage results in a second (faster) relaxation mechanism in addition to the disentanglement

dynamics, $\mu > 1$. The parameter $\epsilon = \lambda_B/\lambda_A$ is the ratio of the relaxation time of the short species B to that of the long species A, for entangled long chains $\epsilon \ll 1$. The number densities have been scaled by the equilibrium number density of species A so that the equilibrium values are $n_A^0 = 1$, $n_B^0 = \sqrt{2c_{Aeq}/c_{Beq}}$ where, as noted above, $c_{Aeq} = \mu - 1$.

The nondimensionalization of the governing equation set is given by the following: total stress $\boldsymbol{\tau} = \boldsymbol{\tau}'/G_o$, where G_0 is the plateau modulus, time $t = t'/\lambda_{eff}$, the scaled spatial variable $r = (R - R_i)/(R_o - R_i) = (R - R_i)/H$, where H is the gap width calculated as the difference of the radius of the outer cylinder R_o and inner cylinder R_i and velocity $v = v'\lambda_{eff}/H$. With the dimensional velocity of the inner wall being denoted as V', the dimensionless velocity at the moving wall is $v(0) = V'\lambda_{eff}/H = De$, i.e. the Deborah number or dimensionless measure of the 'flow strength'. In the rest of this paper, De is also referred as the dimensionless apparent shear rate. This nomenclature is chosen to agree with that used in the previous papers [22, 27, 28, 29, 30]. Contemporary approved terminology for steady shearing flow would be to call this parameter the Weissenberg number, Wi [34]. We define $p = H/R_i$ as a measure of the curvature of the device. As $p \to 0$ the flow approaches a rectilinear plane Couette flow. The tensors $\mathbf{A}, \mathbf{B}$ are the (scaled) second moments of the configuration distribution function for each species and the total micellar stress is $\boldsymbol{\tau}_p = -\mathbf{A} - 2\mathbf{B} + (n_A + n_B)\mathbf{I}$. The dimensionless diffusivity of each species is defined as $\delta_A = \lambda_A D_A/H^2$ and $\delta_B = \lambda_A D_B/H^2$ respectively, in which D_A and D_B are the dimensional diffusivity.

These equations for the number densities and the stresses of each species are

coupled to the equations of conservation of mass:

$$\nabla \cdot \mathbf{v} = 0 \tag{3}$$

and conservation of momentum:

$$E^{-1}\frac{\partial v}{\partial t} = -\nabla \cdot (P\mathbf{I} - \beta\dot{\boldsymbol{\gamma}} + \boldsymbol{\tau_p}) \tag{4}$$

where $\boldsymbol{\tau} = \boldsymbol{\tau_p} - \beta\dot{\boldsymbol{\gamma}}$ is the total stress, that is the stress from the wormlike micellar species and the stress from the solvent. The momentum equation introduces two new dimensionless parameters, the elasticity number $E = \lambda_{eff}\eta_p/\rho H^2$, which is a ratio of the effective relaxation time of the fluid λ_{eff} to the inertial diffusion time $t'_{diff} = \rho H^2/\eta_p$, and $\beta = \eta_s/\eta_p$ which is a ratio of the solvent viscosity to the zero shear rate viscosity of the mixture.

3 Results of the VCM Model in Shear Deformation

We consider unidirectional shear flow in a Taylor-Couette geometry with flow in the θ direction and variations only in the radial direction r. Conservation of mass is automatically satisfied by this unidirectional formulation. The constitutive equations and the momentum equation are solved numerically using a spectral method. The spatial variable is discretized with Chebyshev polynomials and the resulting system of differential-algebraic equations is solved using a multistep backward differentiation formula [35]. The number density of each species, n_A, n_B, satisfies a no flux boundary condition at both the inner and outer cylinders [22, 29] . The stress of each species, $\mathbf{A}$, $\mathbf{B}$, also satisfy a no flux boundary condition. As in [22, 27, 28], the velocity at the inner cylinder is written in dimensionless form as $v_{inner} = De\tanh(at)$ mimicking

the motion of the inner cylinder during a start-up experiment. The parameter a measures how rapidly the inner cylinder reaches its desired speed. In most of our computations we use $a = 10$ which is of the same order as the experiments [7]. In Section 3.3 the effect of varying a on the velocity profile and stress field at steady state is briefly discussed.

For a range of shear rates $\dot{\gamma}_1 < \dot{\gamma} < \dot{\gamma}_2$ the velocity profile exhibits a kink at the spatial position where the shear-rate bands meet. To better resolve the kink region, an adaptive spectral method with transformed Chebyshev points is used. The following conformal mapping [36] redistributes the Chebyshev grid points so that the points are clustered towards the position of the kink:

$$g(r) = d + \kappa \sinh \left[\left(\sinh^{-1} \left(\frac{1-d}{\kappa} \right) + \sinh^{-1} \left(\frac{1+d}{\kappa} \right) \right) \frac{r-1}{2} + \sinh^{-1} \left(\frac{1-d}{\kappa} \right) \right].$$

(5)

In Equation (5) κ is a parameter that determines the density of the points centered around d. The position of the kink and the sharpness of the kink (as it develops) are functions of the time t, spatial position across the gap r and apparent shear rate De, hence d and κ are functions of these variables. The details of the implementation of the method can be found in [36].

The values of the parameters in the model are chosen by reference to experimental data. A detailed rheological fitting can be found in [7, 24]. Parameters were determined by Small Amplitude Oscillatory Shear (SAOS) and step strain experiments [7, 24] on a mixture of CPyCl/NaSal added to water. The constitutive parameters can vary slightly with each preparation batch due to small variations in purity [37]. We have chosen representative parameters within the experimental ranges, namely $\mu = 5.6$, where $\mu = \lambda_A/\lambda_{eff}$ is the ratio of the relaxation time of species A to the effective relaxation time of

the system (including breakage), and the contribution to the total shear stress from the second short species is $\mu \epsilon n_B^0$ which is of order 10^{-3}. We consider ξ =0.7, but also study how changing the value of this single nonlinear parameter, which governs the magnitude of the nonlinear breakage terms, affects the steady state results. The curvature parameter p is determined by the specific experimental test apparatus. In general $0.04 \leq p \leq 0.08$ [6, 38, 1]. We initially compute with $p = 0.1$, but we also investigate the effect of varying p. We choose the effective diffusion parameters for each species to be identical $\delta_A = \delta_B = \delta$ and typical values are taken in the range $10^{-5} < \delta < 10^{-1}$ [29]. Numerical computation shows that the contributions from the $\nabla\nabla : \mathbf{A}$ and $\nabla\nabla : \mathbf{B}$ terms in the number density equations are negligible for this range of δ. With these choices, $\frac{D(2n_A+n_B)}{Dt} = 2\delta\Delta^2(2n_A + n_B)$. Given equilibrium initial conditions and no flux boundary conditions at the walls, the total number of short segments whether joined or not, remains a constant in space and time.

3.1 Model predictions in steady state shear flow

Fig. 1 shows a typical inhomogeneous flow curve predicted by the VCM model under shear rate controlled conditions (blue asterisks joined by broken line). The green solid curve is the corresponding rheometric (homogeneous) flow curve calculated with the assumption that there is no spatial variation in the kinematics. The decreasing portion of this flow curve, between the local maximum at $\dot{\gamma}_M$ and the local minimum at $\dot{\gamma}_m$, is unstable. This conclusion has been shown for the single species, PEC, model in [22]. In the VCM two species model with concentration coupling, we have checked the stability of the homogeneous base flow subject to inhomogeneous perturbations in a circular

12

Couette geometry. The region of instability is still the decreasing portion of the steady state flow curve even with inclusion of normal stresses τ_{rr} and $\tau_{\theta\theta}$, which is in contrast with the d-JS-ϕ model [14]. Therefore, when a nominal shear-rate is prescribed corresponding to this decreasing portion of the flow curve, the velocity profile splits into two regions of distinct shear rates, each located along a locally increasing (stable) portion of the curve, thus forming a stress/strain-rate plateau as shown by the asterisks. The plateau starts at a shear rate $\dot{\gamma}_1$ and ends at the higher shear rate $\dot{\gamma}_2$ denoted in Fig. 1. For apparent shear rates in the range $\dot{\gamma}_1 < De < \dot{\gamma}_2$, the total dimensionless shear stress is roughly a constant $\tau_{r\theta} \approx 0.7$ for this choice of parameters. When the apparent shear rate is below $\dot{\gamma}_1$ or above $\dot{\gamma}_2$, the shear stress increases linearly with shear rate. We note that there is a small variation (or vertical offset) between the values of the stress at a given shear rate for linearly increasing portion of the inhomogeneous and homogeneous flow curves, we will show later in Section 3.2 that this variation is due to curvature effects and this variation decreases as the curvature p decreases. The dashed black line is the contribution to the stress from species B, that is $2B_{r\theta} = 2(n_A^0 + n_B^0/2)\mu\epsilon\dot{\gamma}_{r\theta}$, which is the primary contribution to the shear stress in the high shear rate region. Unlike single species models, such as the PEC model [22], or the Johnson-Segalman model [39], the additional solvent contribution in the VCM model, given by $\eta_s\dot{\gamma}'_{r\theta}$ in the dimensional form, is chosen to be water as opposed to a coarse-grained more viscous Newtonian solvent. The weakly viscoelastic B species also contributes to the linear viscoelastic response of the system. For a comparison of the prediction for G' and G'' and experiments see [7].

The velocity profiles across the gap for selected values of the apparent shear rates in the plateau region of Fig. 1 are shown in Fig. 2(a). For apparent
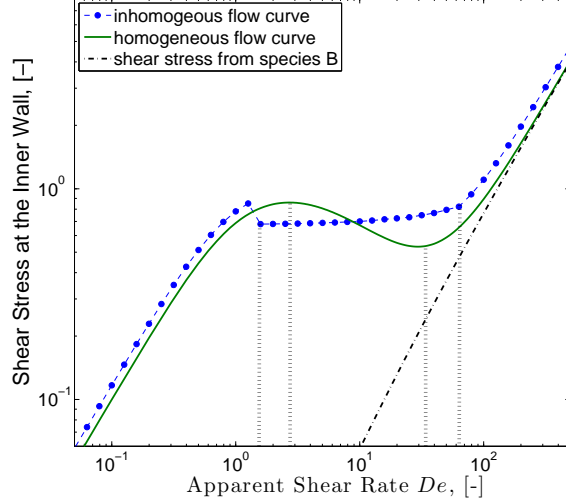
Fig. 1. The dimensionless steady state flow curve of the VCM model for: $\xi = 0.7$, $\mu = 5.7$, $\epsilon = 4.5 \times 10^{-4}$, $n_B^0 = 1.13$, $\beta = 6.8 \times 10^{-5}$, $\delta_A = \delta_B = \delta = 10^{-3}$, $p = 0.1$.

shear rates in this region, a two-banded structure is observed with a high shear rate towards the inner (moving) wall and a low shear rate towards the outer (stationary) wall. The location at which the velocity profiles with the two different shear rates meet represents a "kink" or shear localization between the two bands. Mathematically, the location of the kink can be determined either by finding the local maximum in the second derivative of the velocity profile, or by locating the maximum of the first derivative of the shear stress $A_{r\theta}$ [29]. Here we use the local maximum of the second derivative of the velocity profile as the kink location, r_k. As the value of the apparent shear rate imposed on the flow increases, the kink moves outwards towards the outer cylinder until the high shear rate region spans the entire gap. The inset of Fig. 2(a) shows that the location of the kink varies almost linearly with the value of the apparent shear rate De which is consistent with experimental observations [2, 40]. Fig. 2(b) shows the number density profile of the long species A across the gap at the same selected apparent shear rates. In the high shear rate region the long
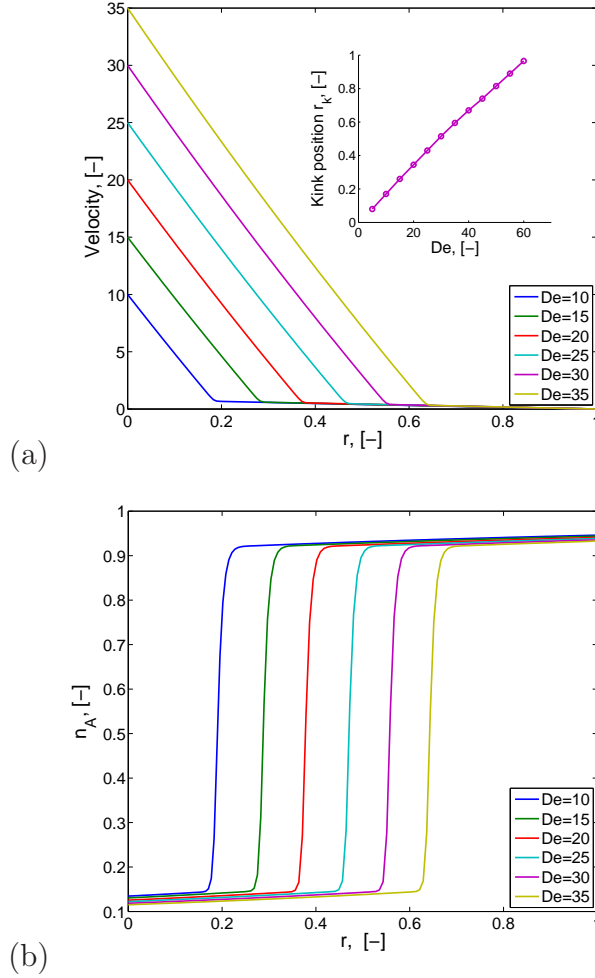
(a)

(b)

Fig. 2. (a) Inhomogeneous velocity profile across the gap as the imposed shear rate $De = V'\lambda_{eff}/H$ is increased. (b) Number density distribution of the species A across the gap. The model parameters are the same as those in Fig. 1.

species A has broken to form two shorter segments of species B, therefore the number density of species A stays at a low level ($n_A \approx 0.12$). By contrast, in the low shear rate region the (scaled) density n_A is close to unity, its initial equilibrium level. The total number density $2n_A + n_B$ remains constant across the gap (determined by the initial conditions).

The time evolution of the shear stress and the first normal stress difference
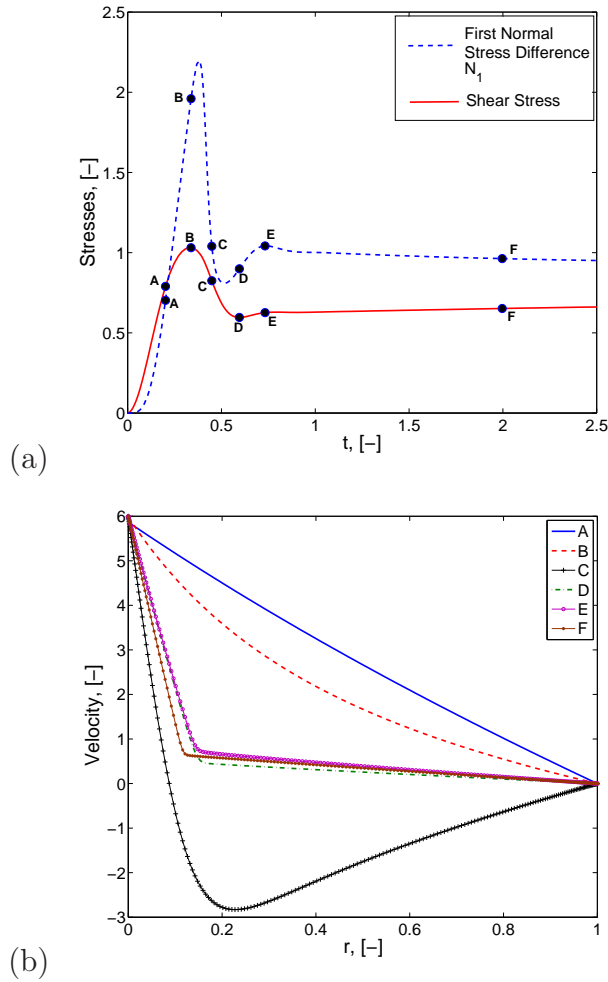
(a)

(b)

Fig. 3. (a) Shear stress and the first normal stress difference at the inner cylinder after start up of the flow. (b) Velocity profiles across the gap for selected times in (a). $De = 6$, $a = 10$. The model parameters are the same as those in Fig. 1.

N_1 at the inner cylinder, after start up of the flow, and the corresponding velocity profiles at selected times are shown in Fig. 3(a). For this value of the Deborah number ($De = 6$), both the shear stress and the normal stress difference exhibit an overshoot and a subsequent undershoot before they reach their steady state values. The overshoot in the shear stress occurs before the overshoot of the first normal stress difference. When the viscoelastic stresses pass through their maximum values, the fluid elastically "unloads" and this

16

results in a transient elastic recoil during which a velocity profile with local negative values is observed (see for example Profile C in Fig. 3(b)). This result is very similar to experimental PIV observations in micellar fluids and to what the simpler PEC model predicts [22]. The difference between the PEC and the VCM models is that in the VCM model, the elastic recoil is more pronounced due to an enhanced breakage of the long species A.

Close inspection of Fig. 3(a) shows that the initial growth in the shear stress is not linear in time. This short time response is due to the prescribed time dependent start up of the wall velocity given by $v_{inner} = De \tanh(at)$. The wall velocity takes a time on the order of $1/a$ to reach its final steady state value. For a value of $a = 10$, it takes a time $t \approx 0.15$ for the velocity to reach 90% of its final value. If we let a become very large, for example $a = 100$, then the initial expected linear response of the fluid shear stress with time is recovered.

The shape of the steady state flow curve varies when the parameters in the constitutive equations, specifically ξ (the single nonlinear model parameter which governs the strength of the nonlinear breakage rate of species A), and the ratios of the time constants $\mu = \lambda_A/\lambda_{eff}$ and $\epsilon = \lambda_B/\lambda_A$, change their magnitude. A discussion of the effects of varying these parameters in a homogeneous/rheometric flow can be found in [24]. Here we concisely assemble the effect of variations of these parameters for fully inhomogeneous flow conditions in Fig. 4 and 5.

In Fig. 4(a) we show the flow curves for several values of $\xi = 0.3, 0.5$ and 0.7. It is clear that this parameter changes the steady state flow curves only by raising or lowering the position of the plateau. Larger values of ξ lower
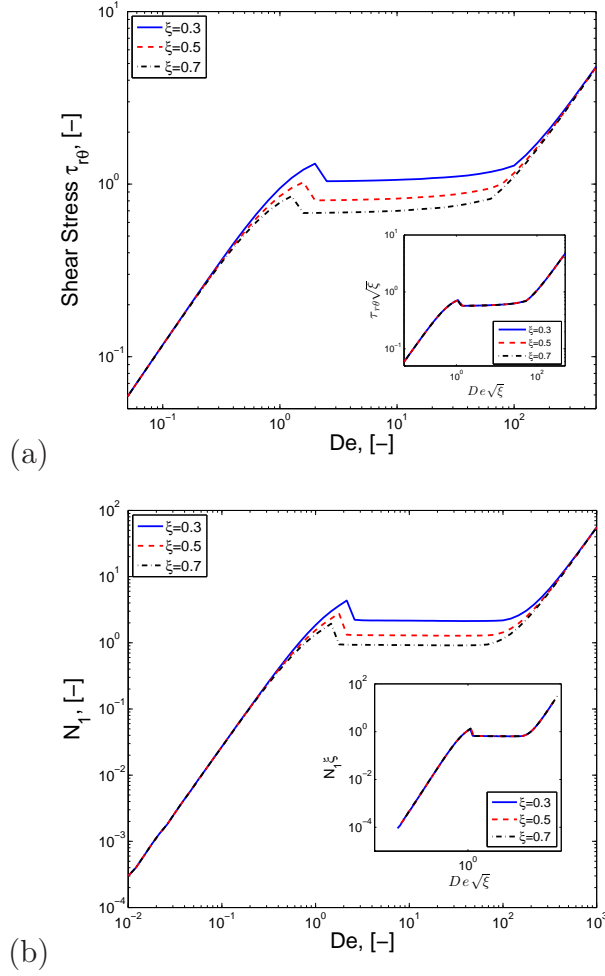
(a)

(b)

Fig. 4. The steady state shear stress (a) and the first normal stress difference (b) as a function of the apparent shear rate for the inertialess VCM model with variation the nonlinear breakage parameter ξ. All other parameters remain the same as in Fig. 1. The insets of each figure show the scaled flow curves to be independent of the nonlinear parameter ξ.

the plateau, thus causing the plateau region to start and end at lower values of the apparent shear rates as compared to the values obtained for a smaller value of ξ. However, the plateaus have the same length and are parallel to each other. Fig. 4 (b) shows the first normal stress difference, N_1, as a function of apparent shear rate De for the same three values of ξ. For the VCM model, N_1

increases quadratically with respect to the shear rate in the two linear regions of the flow curve. In the plateau region of the flow curve, N_1 at the inner wall also shows a plateau in Taylor-Couette flow. This result is not consistent with what is found in experiment in a cone-plate device [7].

Closer inspection of the individual components of the constitutive equations of the VCM model in steady shear flow shows that if the shear stresses from each species and the shear rate are rescaled by $\sqrt{\xi}$ and N_1 is rescaled by ξ (so that $A_{r\theta,new} = A_{r\theta}\sqrt{\xi}$, $B_{r\theta,new} = B_{r\theta}\sqrt{\xi}$, $\dot{\gamma}_{r\theta,new} = \dot{\gamma}_{r\theta}\sqrt{\xi}$ and $N_{1,new} = N_1\xi$) then the rescaled equations are independent of ξ in the inertialess case (ξ will be present in the rescaled elasticity number E in the momentum equation). The insets of Fig. 4(a) and Fig. 4 (b) show the consequence of this independence, the flow curves for different values of ξ superpose when rescaled as described above. This change of variable is very similar to the simplification that have been noted for the diffusive Johson-Segalman (dJS) model [42, 43], for which the constitutive parameter a can be scaled out of the equation set using a suitable rescaling.

The effect of varying the parameter μ is shown in Fig. 5(a). In the VCM model, μ is the ratio of the stress relaxation time of the species A to the effective relaxation time of the mixture ($\mu = \lambda_A/\lambda_{eff} = 1 + c_{Aeq}$) and thus specifically provides a measure of the rate of breaking in the long species A close to equilibrium conditions. The curves show that for smaller values of μ, the plateau is lower and ends later than for a larger μ. The three parts of the flow curve, i.e. the first linear regime, the plateau, and the second linear (high shear rate) portion are determined primarily by, respectively, $A_{r\theta}$, a combination of $A_{r\theta}$ and $B_{r\theta}$, and $B_{r\theta}$. Therefore a lower and longer plateau means the contribution to the total shear stress from the short species B is
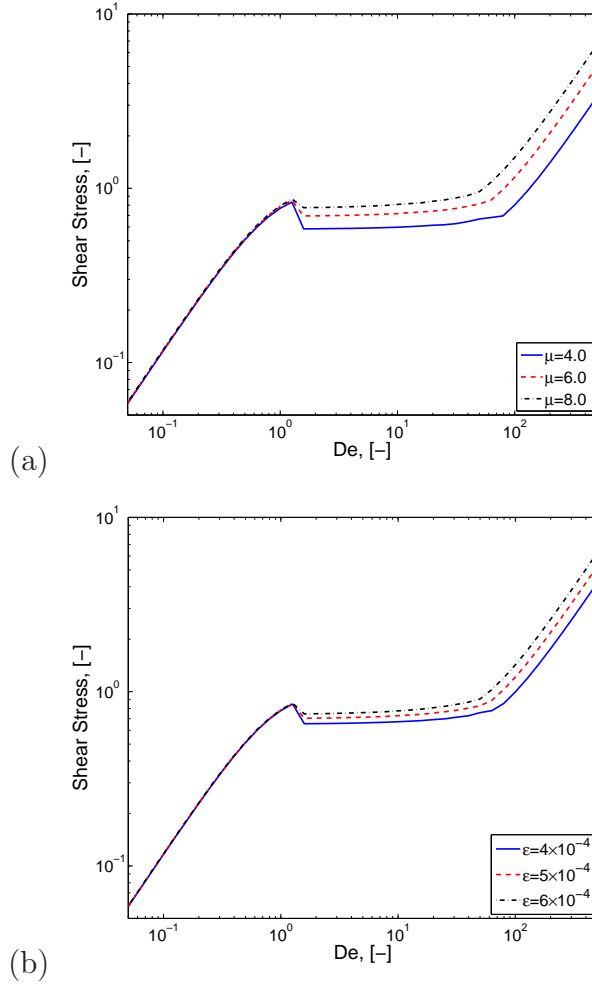
Fig. 5. The steady state flow curve for the inertialess VCM model with variation of the parameters (a) $\mu = \lambda_A/\lambda_{eff}$ and (b) $\epsilon = \lambda_B/\lambda_A$ for a fixed value of $a = 10$. All other parameters remain the same as in Fig. 1.

smaller and less significant until higher shear rates. This is consistent with a smaller breakage rate of the long species. The effect of $\epsilon = \lambda_B/\lambda_A$, i.e. the ratio of the relaxation time of the short species B to that of the long species A, on the steady state flow curve is similar to that of μ as expected, since for a fixed value of λ_B the magnitude of ϵ varies with λ_A and hence with λ_{eff}. The curves for varying ϵ are shown in Fig. 5(b). For larger ϵ the plateau is higher and ends earlier corresponding to larger viscoelastic contribution to the total

20

stress from the short chain 'B' species.

3.2 Curvature Effects

Although the Taylor Couette geometry provides a good approximation to a planar shearing flow in the narrow gap limit, the curvature p of the geometry still has important effects on the shape of the flow curve and the width of the shear banding plateau between $\dot{\gamma}_1$ and $\dot{\gamma}_2$. Fig. 6(a) shows steady state solutions for the VCM model equations for different values of the curvature parameter $p = 0.01, 0.05$ and 0.1. The dotted line (green) represents the homogeneous flow solution, that is the viscometric flow curve. In the two linear regimes, as p decreases, the flow approaches the viscometric limit; variations in the velocity field resulting from curvature decrease monotonically and the velocity profile becomes closer to linear across the gap. The small deviation from linearity in the velocity field results in small $O(p)$ variations in the flow curve so that the difference between the full (inhomogeneous) flow curve and the limiting homogeneous solution decrease as $p \to 0$ (see inset for better view).

The effect of the curvature on the width and the shape of the plateau has been noted previously by Olmsted et.al. [39]. From Fig. 6(a) it is clear that larger values of the curvature p result in longer plateaus, that is, the plateau starts at lower values of the apparent shear rate and ends later, while smaller values of p lead to shorter plateaus. On the homogeneous flow curve, the locally decreasing part of the curve with $\partial\tau_{r\theta}/\partial De < 0$ is linearly unstable (see the dashed line of the nonmonotonic flow curve in Fig 6(b)). Ideally, in a homogeneous planar shearing flow, when the apparent shear rate De is between
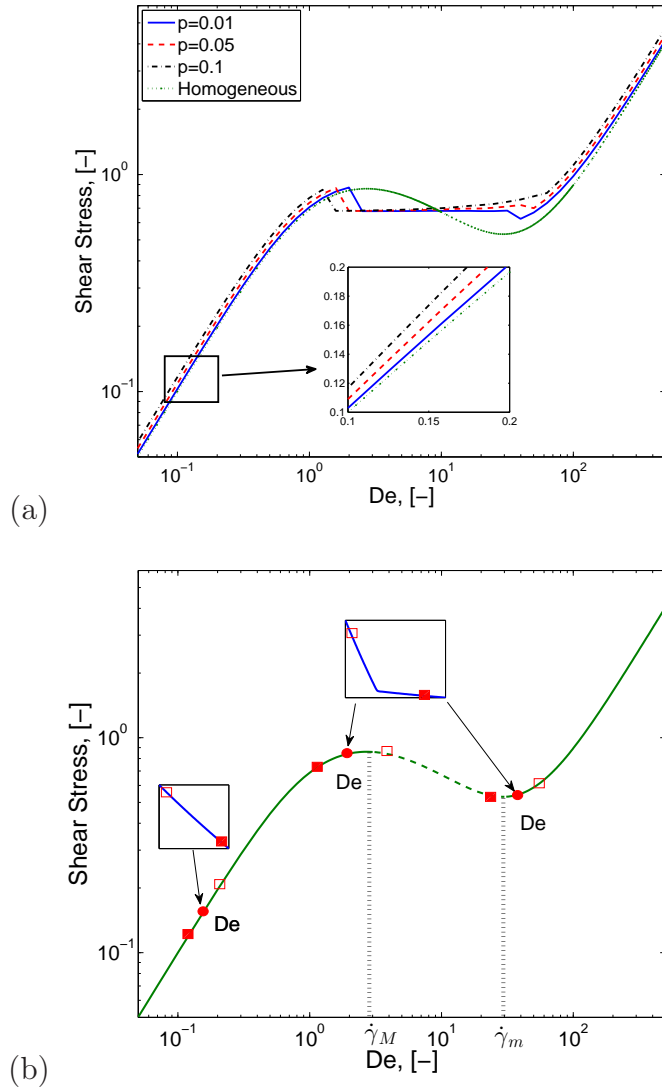
21

Fig. 6. (a) The steady state flow curve for the inertialess VCM model for different values of the curvature $p = \frac{R_o - R_i}{R_i}$. We keep $a = 10$, $\delta = 0.001$ and all other parameters remain the same as in Fig. 1. (b) Local spatial variations in the shear rate across the gap for selected values of the imposed dimensionless shear rate De. The insets show local velocity profiles in which the hollow and filled squares show the corresponding maximum and minimum values of the shear rate ($\dot{\gamma}_i$, $\dot{\gamma}_o$) of the profile respectively.

the local maximum $\dot{\gamma}_M$ and local minimum $\dot{\gamma}_m$ of the homogeneous flow curve, a plateau occurs. However, this is not the case in the Taylor Couette geometry. In a planar geometry, the local shear rate is a constant value across the gap, $\dot{\gamma}_{local} = \lambda_{eff}V'/H = De$. However, when there is curvature present, even in the linear regimes, the local shear rate across the gap is a function of space [22]. The local shear rate $\dot{\gamma}_{r\theta}(r)$ varies between $\dot{\gamma}_o$, $\dot{\gamma}_i$ with the maximum shear rate occurring at the inner moving wall $(\dot{\gamma}_i \equiv \dot{\gamma}_{r\theta}(r = 0))$ and the minimum shear rate at the fixed outer wall $(\dot{\gamma}_o \equiv \dot{\gamma}_{r\theta}(r = 1))$ as shown in Fig. 6(b) by the hollow and filled symbols respectively. Obviously, the span $\Delta\dot{\gamma} = (\dot{\gamma}_i - \dot{\gamma}_o)$ of the local shear rates encountered across the gap increases for larger p. The velocity profile starts to shearband to form a 'kinked' or banded structure not when the nominal or average value De lies in the unstable region, but when the maximum shear rate $\dot{\gamma}_i$ enters the unstable region, that is when $\dot{\gamma}_i > \dot{\gamma}_M$. Since $\Delta\dot{\gamma} > 0$ for the Taylor Couette geometry, this means the plateau begins before the apparent shear rate De itself reaches the unstable region at $\dot{\gamma}_M$, as indicated by the inset velocity profile in Fig. 6(b). For the same reason, shear banding persists till the minimum local shear rate in the gap no longer lies in the unstable region, i.e., $\dot{\gamma}_o > \dot{\gamma}_m$. Since $\Delta\dot{\gamma}$ increases for larger values of the curvature p, it is clear that the extent of the shear banding plateau must grow with increasing p.

The effect of the geometry on the steady state flow curve measured in worm-like micellar fluids can also be investigated though experimental results carried out in different flow configurations. To circumvent problems associated with motor response times, fluid inertia and edge fracture in torsional flow devices, it is often convenient to use a Poiseuille channel flow for high shear rate experiments [44, 45, 46]. In a slit geometry the flow is controlled through the pressure

drop imposed along the channel, as opposed to an imposed wall driven velocity or apparent shear rate as in at a Taylor-Couette or cone-plate geometry. Although the curvature p in a rectangular channel (slit geometry) is now zero, it was shown in [29] that a new dimensionless geometric measure, namely the characteristic length of the channel $l_p = G_0 L/\Delta p'$, takes its place. This parameter appears in the momentum equation in the form $\mathcal{P} = \Delta p' H/(G_0 L) = H/l_p$. A channel flow experiment is carried out at a prescribed $\mathcal{P}$. Using PIV measurements, the local shear rate and stress are determined at locations across the gap and graphed to reconstruct the local flow curve at that value of $\mathcal{P}$. It has been shown in [29] that the interplay between $\mathcal{P}$ and the diffusivity parameter δ affects the form of the flow curve reconstructed from a channel flow experiment. In particular, for a fixed value of δ, as $\mathcal{P}$ increases the 'plateau' in the flow curve develops an increasingly positive slope.

Both parameters $\mathcal{P}$ and δ depend on the height of the channel ($\mathcal{P} = \Delta p' H/(G_0 L)$ and $\delta = \lambda_A D_A/H^2$) so that experiments carried out using channels of different heights, or in the same channel but for different values of the applied pressure drop along the channel, will exhibit different flow curves. In [29], it was shown that the flow curves collapse onto a single master curve only if the parameter combination $\mathcal{P}\delta^{1/2}$ is held constant between geometries and experiments. In Fig. 7 we show experimental data collected in a torsional rheometer (open squares, AR-G2) using a cone and plate fixture at low shear rates, and in a rectilinear microchannel (mVROC, filled squares) at higher shear rates using the same fluid, a CPyCl-NaSal mixture with concentrations of [100:60] mM [47]. The microchannel experiments were carried out by varying the imposed pressure gradient $\mathcal{P}$ to obtain the desired flow rate. It is clear that the locations of the shear banding plateaus do not agree; instead the plateau value
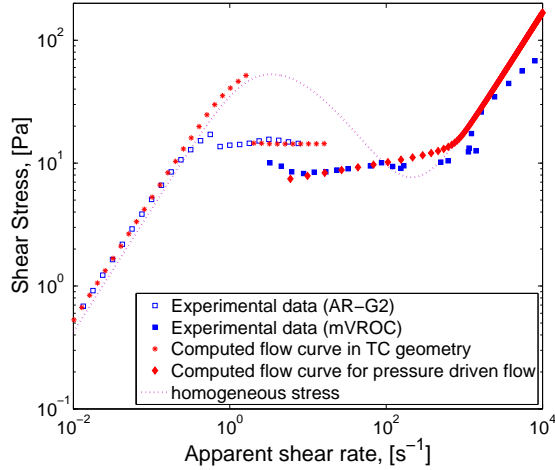
Fig. 7. The steady state flow curves for a single wormlike micellar fluid obtained from two different experiments [47]: using an AR-G2 torsional rheometer and mVROC microfluidic device, respectively, plus corresponding simulation for Taylor-Couette flow and pressure driven flow. In the simulation: $\beta = 2.2 \times 10^{-5}$, $n_B^0 = 1.13$, $\mu = 1.8$, $\epsilon = 7 \times 10^{-5}$, $\xi = 0.1$, $p = 0.15$, $\delta = 0.001$. The value of the dimensionless pressure difference is $\mathcal{P} = 30.9$ for the pressure driven flow [48].

in the microchannel is lower than the value observed using the cone-plate fixture. By contrast, in non shear banding fluids excellent overlap between the two flow curves obtained with the two devices are obtained [44]. Flow curves for the VCM model were simulated with the same parameter values as in the experiments using the known material parameters ($G_0 = 27.2$ Pa, $\lambda_{eff} = 1.67$ s), the additional constitutive parameters in the model were fit so that the monotone increasing portions of the simulation and the experiment agreed. The simulations were carried out for a Taylor-Couette geometry at low shear rates, and for a rectangular channel at fixed $\mathcal{P}$ at higher shear rates [48]. For the particular values of p (for the Taylor-Couette flow), and $\mathcal{P}$ (for the microchannel flow), the model predictions agree with the experimental results along much of the plateau. The VCM model simulation shows a larger over-

shoot at the low shear rate end of the plateau than is observed experimentally in the cone-plate geometry possibly because of the more complex transition to shear banding expected in a cone-plate device [7, 49].

3.3 Long Time Memory of Short Time Start-Up Conditions

A plot of the steady state flow curve obtained after a transient ramp up from initial rest conditions shows that the total shear stress in the fluid "overshoots" or exceeds the plateau value at the low shear rate end of the plateau near $\dot{\gamma}_M$. This is particularly clear when the curvature p is small (see the flow curve for $p = 0.01$ in Fig. 6). This local maximum in the steady state flow curve has been documented in a number of experiments for different micellar fluid [1, 7]. As reported in those experiments, if the wall velocity is ramped up to its final value, the flow curve exhibits a shear stress overshoot before entering the plateau region of the curve. By contrast if the wall velocity was ramped down to its final value this overshoot disappeared, and so this overshoot represents a metastable, history-dependent branch of the flow curve.

To explore whether the existence of this overshoot is dependent on the initial ramp conditions, we show two steady state flow curves in Fig. 8 evaluated for different values of the step rate ramp parameter a (Fig. 8 (a) is for a faster ramp $a = 10$ and Fig. 8 (b) is for a slower ramp $a = 1$). In each figure the hollow circles (blue) represent the steady state solution for a shear rate ramped up from equilibrium (that is $v_{inner} = De \tanh(at)$, with other variables initialized at their equilibrium conditions), the asterisks (red) represent the steady state flow curve for a shear rate which is ramped down from a steady state at a higher wall velocity using the same value of a (here we use $v_{inner} =$
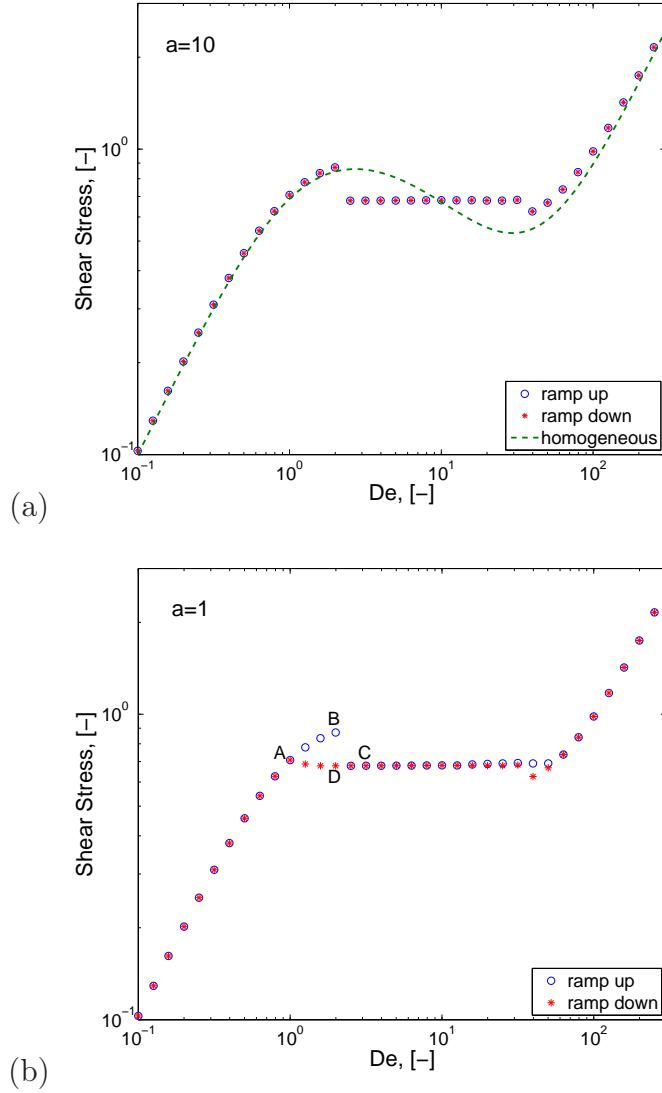
(a)

(b)

Fig. 8. The effect of varying the ramp rate parameter a on the steady state flow curve for the inertialess VCM model: (a) for a fast ramp up or down ($a = 10$), the steady state curves are indistinguishable. The green dashed line is the homogeneous response; (b) for a slow ramp up or down ($a = 1$) the profiles obtained during the ramp up and ramp down are different. In this figure the labeled points correspond to A: ramp up, $De = 1$; point B: ramp up, $De = 2$; point C: ramp up, $De = 3$; point D: ramp down, $De = 2$. In both figures the gap curvature and diffusivity are held constant at $p = 0.01$, $\delta = 0.001$. All other parameters remain the same as in Fig. 1.

$500 + (De - 500) \tanh(at)$ and the initial values of other variables are their values at the steady state value obtained after a ramp up to $De = 500$). The number $1/a$ represents roughly the time for the velocity applied at the inner wall to reach its final (imposed) value. Small values of a correspond to a slow ramp whereas large values a correspond to a fast ramp. A ramp with $a = 10$ is almost complete at a dimensionless time of 0.1, well before the system has time to relax (note that for a typical De on the plateau, elastic recoil is well in progress at roughly $t \sim 0.4$, see Fig. 3). On the other hand, a ramp with $a = 1$ is not complete until an elapsed time of $t \sim 1$, well after relaxation to a banded state has occurred. Thus in the latter case the dynamical system locally equilibrates to shear rates along the upwards ramp or decay (during the ramp down) hence effectively experiencing all shear rates between the initial value and the final value. The two flow curves shown in Fig. 8 for each pair of simulations are coincident *except* at the beginning of the plateau region and at the end of the plateau region. The results in Fig. 8(b) show that for a slow ramp up and ramp down ($a = 1$), there is hysteresis at the low shear rate end of the plateau; i.e. there is an overshoot in the stress if the system reaches steady state through a ramp-up condition (hollow circles), but no overshoot when ramping down (red asterisks). Similarly, at the high shear rate end of the plateau under ramp-down conditions there is a small undershoot, while for ramp up there is no undershoot. For a fast ramp up or a fast ramp down ($a = 10$, Fig. 8(a)), there is both an overshoot at the low shear rate end of the plateau and an undershoot at the high shear rate end of the plateau.

The hysteresis observed at the beginning of the plateau for slow ramp up conditions ($a = 1$) is consistent with experiments [1, 50]: i.e. a stress overshoot is observed in the flow curve at the beginning of the plateau when the shear
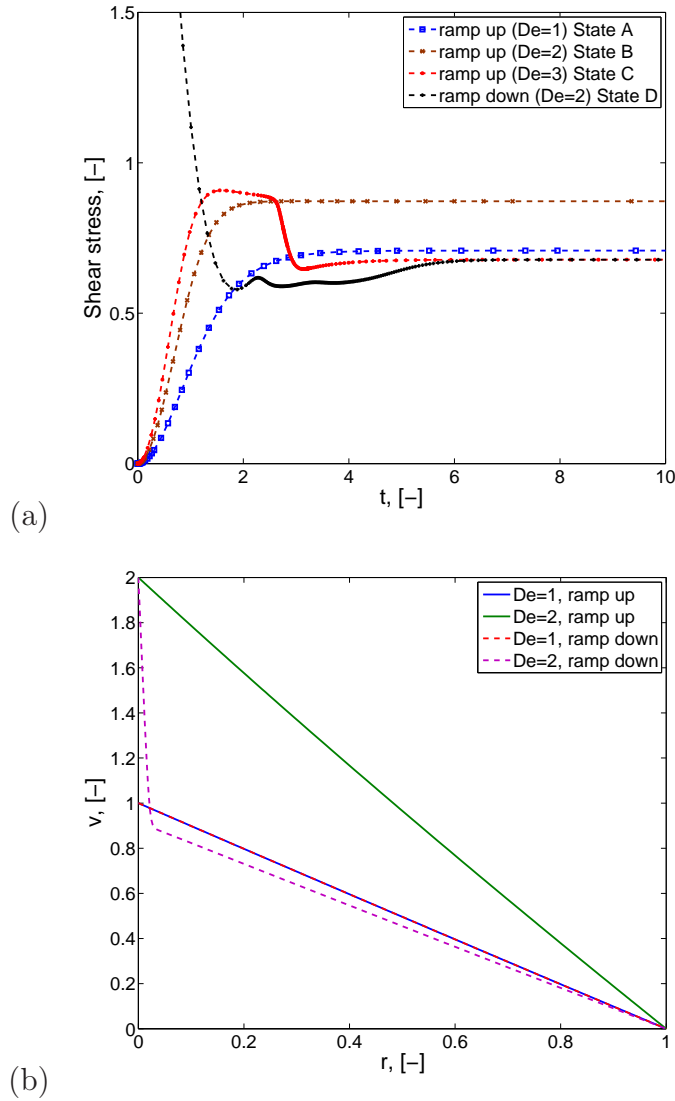
(a)

(b)

Fig. 9. (a) The transient stress growth curves as a function of time for the inertialess VCM model in the overshoot region of Fig. 8(b). In the figure we hold $p = 0.01$ and $a = 1$. (b) The corresponding steady state velocity profiles for $De = 1$ and 2 in ramp up and ramp down flow conditions.

rate ramps up but no such overshoot is observed when the shear rate is ramped down. In Fig. 9 the transient stress responses for the VCM model for apparent shear rates of $De = 1, 2, 3$ during the ramp up, and $De = 2$ during the ramp down are plotted. At $De = 1$ (state A), there is no shear banding, the

29

shear stress smoothly approaches its steady state. At $De = 3$ (state C), the stress overshoots in time, thereafter decaying eventually to reach its steady state value. For $De = 2$, during the ramp up (state B), the stress increases monotonically to the steady state and then remains constant with no time overshoot and no band formation (see Fig. 9(b) for the steady state velocity profile), however, when the flow is ramped down to the same value of $De = 2$ (state D), the shear band has already been formed (at the initial, much higher shear rate) and the banding persists. It is for this reason that [1] refer to the overshoot branch near $De = 2$ as a metastable branch of the steady state flow curve: If the flow starts from a linear initial condition (ramp up), it will take an infinite time for the bands to nucleate and thus for the shear stress to relax to the plateau stress value; however if shear bands have already been formed in the velocity profile, then the banded structure persists.

As pointed out above the situation for a fast ramp is quite different from that for the slow ramp up as we have shown in 8(a). In this case, for a curvature of $p = 0.01$, the overshoot at the beginning of the plateau is seen for both ramp up and ramp down conditions. The same is true for the undershoot at the right hand end of the plateau. In these cases the ramp is so fast that the final wall velocity is attained well before the stress in the system has relaxed to the steady state profile. The velocity across the gap rapidly reaches its "homogeneous" value at the targeted apparent shear rate. When this shear rate is on the stable portion of the flow curve the system stays on that branch, unbanded. By contrast, in the slow ramp case the system samples all shear rates on the path to the final equilibrium profile.

In [28] the transition to multiple shear banded structures was studied in the presence of fluid inertia. It was shown that multiple banded structures can develop in the transient velocity profiles, and, in the absence of diffusion these can persist to the steady state velocity profiles. This multiple banding arises due to the interaction between the initial inertio-elastic shear wave that propagates across the gap and the nonlinear evolution in the viscoelastic stress field within the fluid which drives the band formation. In our previous study we also considered the effect of diffusion on this multiple banding formation process and showed that the multiple banding events eventually decay to a two banded state when the presence of stress-concentration diffusion in the system is accounted for. In that paper it was shown that the time for the multiply banded velocity to decay to the two banded curve was proportional to $1/\sqrt{\delta}$.

That observation motivates investigation of the effect of varying the magnitude of the diffusion constant on the steady state flow curves. In Fig. 10(a) we show the changes in the steady state flow curve observed for values of $\delta = 10^{-1}$, 10^{-2} and 10^{-3}. The steady state flow curves were obtained for a fast initial ramp rate ($a = 10$). Calculation is carried out for these values of δ to an elapsed time of $O(200)$ well after the steady state is achieved. Note that the small undershoot on the right hand end of the plateau (see Fig. 8) does not survive for a large curvature such as $p = 0.1$ used in this calculation. The effect of diffusion in this parameter range is weak except at the very beginning of the plateau. The overshoot in this region indicates a transition from a homogeneous velocity profile to a banded or kinked profile. This overshoot,
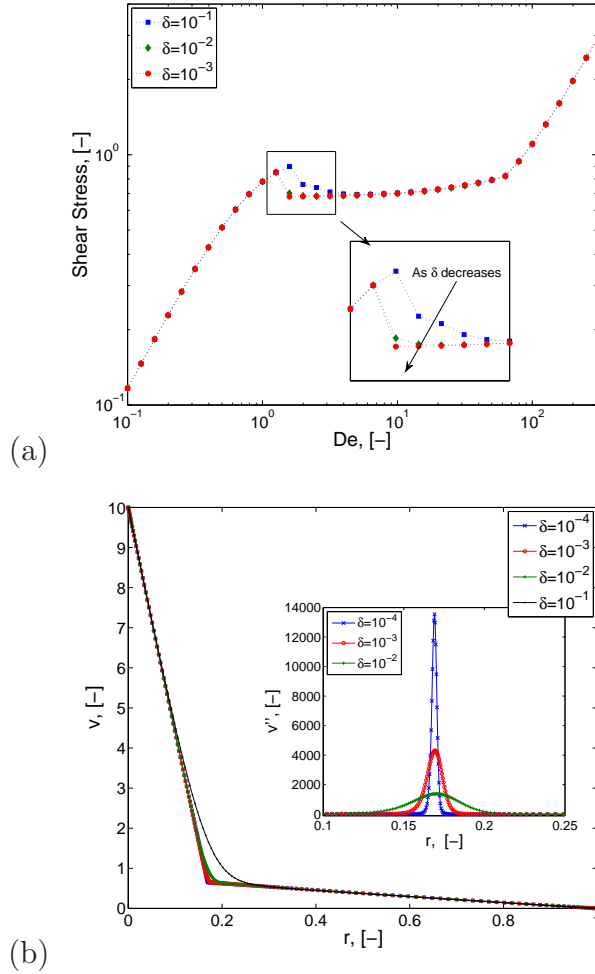
Fig. 10. (a) The steady state flow curve for the VCM model with different values of the dimensionless diffusivity $\delta = \lambda_A D/H^2$. (b) The corresponding velocity profile for $De = 10$ for different values of diffusivity. The inset shows the second order derivative of velocity $v''(r)$. In the simulation we set $p = 0.1$ and $a = 10$. The other parameters are the same as those of Fig. 1.

documented experimentally in [1], smooths out as the diffusion constant increases in the VCM model. In this earlier experimental study, the overshoot is interpreted as a metastable branch with an "effectively infinite relaxation time" [1] for the system which is attempting to form a shear banded state. Also Radulescu et. al [42] attribute the difficulty of forming the shear bands

at the beginning of the plateau to the effect of the wall since at this juncture the band formation initially develops close to the moving inner wall. Because diffusion is a nonlocal effect, such wall-driven effects are stronger for larger diffusion constant. In Fig. 10(b) we plot the simulated VCM model velocity profiles for $De = 10$ for diffusivity values spanning the range $\delta = 10^{-4} - 10^{-2}$. The computations show that for these values of diffusivity the effects of stress-concentration coupling on the velocity profile are located primarily at the kink. Larger values of the diffusivity smooth and broaden the connection between the two bands and their distinct shear rate regions. The spatial extent of the transition region scales with $\sqrt{\delta}$.

In Fig. 11 we show the effect of diffusion on the steady state number density and the stress distribution across the gap for each species. Diffusion smoothes out the sharp transition between the two shear rate bands just as it does to the velocity profiles shown in Fig. 10(b). We have also confirmed numerically that the width of the transition region in the shear stresses scales with $\sqrt{\delta}$, too. The total number density, $2n_A + n_B$, remains invariant across the gap and the total shear stress $\tau_{r\theta} = -(A_{r\theta} + B_{r\theta} + \beta\dot{\gamma})$ always varies as r^{-2}.

3.5   Model prediction in transient shear flow

The elasticity number $E = \lambda_{eff}\eta_p/\rho H^2$ does not have an appreciable effect on the long time (steady state) VCM model behavior when diffusive effects are present, it does have an effect on the transient response of the system. Fig. 12(a) shows the transient response of the total shear stress for different values of E with a fixed diffusivity of $\delta = 10^{-4}$ and a fixed $De = 10$. The responses for the selected values of E differ on time scales smaller than one relaxation
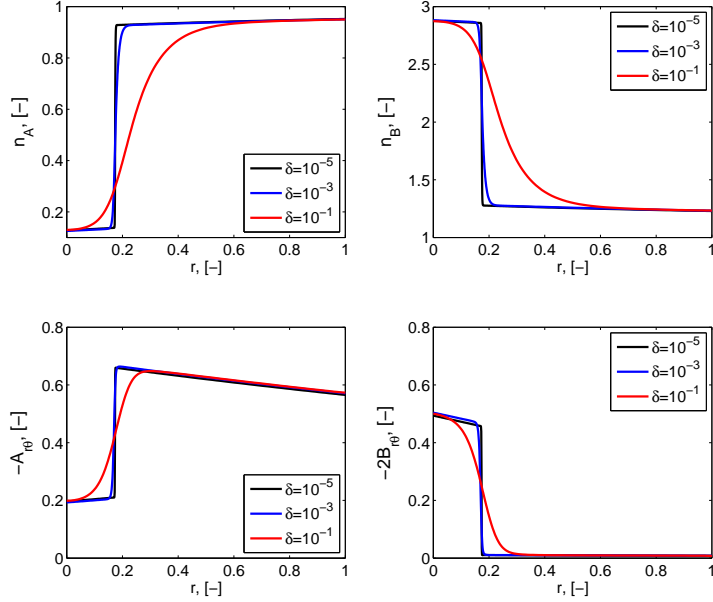
Fig. 11. The effect of changing the dimensionless diffusion parameter δ in the VCM model on the steady state profiles in the banded region at $De = 10$. The top row shows the number density distributions n_A and n_B of species A and B, respectively across the gap. The bottom row shows the shear stress distribution across the gap arising from each species.

time; however, the shear stresses all approach the same steady state at about the same time (see inset). The effects of fluid inertia captured in the elasticity number E primarily modify the short term behavior of the shear stress.

Following the startup of a steady shear flow, there are five distinct time responses as indicated in Fig. 12(a) by Roman numerals. The first stage (region I) corresponds to the initial propagation of an inertio-elastic wave across the gap with characteristic wave speed $\sqrt{E}$. This is particularly noticeable when E is small. Note that in Fig. 12(a), the "shoulder" in Region I is associated with the reflection of the elastic shear wave from the stationary wall. A detailed
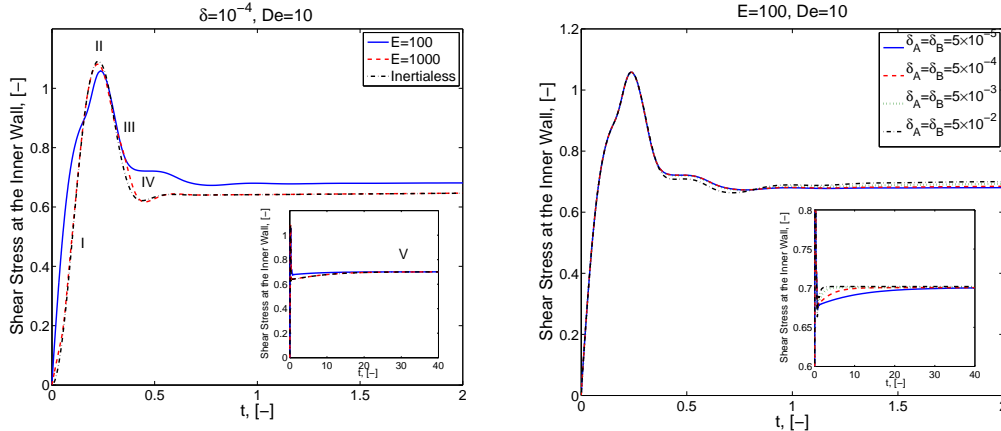
34

Fig. 12. (a) Transient responses in the dimensionless shear responses of the VCM model for fixed value of diffusivity $\delta = 10^{-4}$ and different values of the elasticity number E. (b) Transient shear responses for fixed $E = 100$ and different δ. The insets of both figures show the long term behaviors for $t \leq 40$. Here we keep $a = 10$ and $De = 10$. All other model parameters remain the same as in Fig. 1.

discussion of the elastic wave responses can be found in [28]. Following the shear stress overshoot (region II) there is a period in which the shear stress decreases (region III) and the shear bands develop. In the fourth stage (region IV) , depending on the magnitude of the elasticity number E, the stress may either experience a temporary plateau or an undershoot followed by another overshoot. During the long slow (diffusive) period (region V shown in the inset) the stress gradually increases to approach its steady state value. These different response regions have been documented in experiments by Lerouge. et al [38, 40].

To demonstrate that this long time response in region V is diffusive in character, we show in Fig. 12(b) a set of computations for varying values of δ. Clearly there is minimal effect on the short time shear stress responses resulting from changes in δ. In the case of $E = 100$ all of the profiles show that the

35

stress first increases, then overshoots, then decreases to a short lived plateau followed by an oscillatory approach to the steady state. However, the inset of (b) shows different long term responses for different values of diffusivity δ: both the value of the steady state solution and the time at which the steady state is achieved are dependent on δ; as the diffusivity is decreased the time to reach the final steady state value increases.

To further investigate the VCM time responses in these five stages, the velocity profiles in regions I-V are plotted in Fig. 13 for $E = 100$ and $E = 1000$, respectively. The elasticity number represents a balance of inertial and diffusive time scale and the speed of the inertio-elastic shear wave scales with $\sqrt{E}$ [28]. Note that the response for $E = 1000$, as anticipated, is very close to the inertialess response (see Fig. 12(a)). For the smaller value of $E = 100$, in region I, the inertio-elastic wave propagation (regularized by the diffusive response of the solvent and shorter B chains) is clearly observed (left top figure of 13(a)). It takes a finite time $\Delta t = 1/\sqrt{E} = 0.1$ for the velocity to propagate from the inner cylinder to the outer cylinder. The reflected wave causes an overshoot in the velocity profile near the middle of the gap at $t = 0.15$. This overshoot is not observed for the larger value of E at the same time (left top figure of 13(b)) in which case the speed of the wave is about $\sqrt{E} \approx 32$. By an elapsed of time $t = 0.15$, the effects of the inertio-elastic wave have already been dissipated [28]. The local maximum in the stress (region II) occurs at about $t = 0.23$. At this moment, the velocity at the inner wall reaches its final value. This time scale is related to the value of the ramp parameter a that we use in the simulation (here we use $a = 10$). If the ramp time is shorter (i.e. a is larger), we expect this time to be smaller. During region III, as the shear stress locally decreases, the shear bands are formed. Although

the stresses look similar for each simulation in this region, the velocity profiles evolve quite distinctly for different values of E. For $E = 100$, a transient three-banded structure is formed due to interference of the reflected inertio-elastic wave and the developing stress profile, as we have documented previously [28], while for a larger elasticity number $E = 1000$, multiple bands do not develop. The absence of a multiple banding structure for the larger value of E is again because the reflected inertio-elastic wave has already dissipated by the time the stress overshoots in Region II [28]. Instead, a regular two-banded structure is observed with a prominent elastic recoil in the velocity profile. This elastic recoil has been observed in different models [18, 22] as well as experiments [2, 51]. In region IV, the multiple bands that are initially formed in the $E = 100$ case gradually diffuse away and a steady two banded structure is recovered (left bottom of Fig. 13(a)). This gives rise to the intermediate plateau in the stress responses, while for the $E = 1000$ case, the velocity v_k at the kink location (r_k) oscillates weakly before relaxing to its steady state value (left bottom of 13(b)) which gives rise to the undershoot and overshoot in the shear stress. As the stress profiles gradually approach the final steady state for $t \geq 0.7$, the kink between the two shear bands becomes sharper and its spatial location r_k slowly diffuses inwards slightly toward the moving cylinder. This final diffusion-dominated region is denoted region V for both cases.

The long-time transient responses of the VCM model in the banded regime is determined not only by the diffusivity, but also by the apparent shear rate De imposed at the wall which determines how deeply into the nonlinear banded regime the system is being driven. For the same value of the diffusion constant, when the apparent shear rate (De) is large, the system takes longer to reach steady state (see Fig. 14 and the inset to Fig. 14(a)). To explore this long-
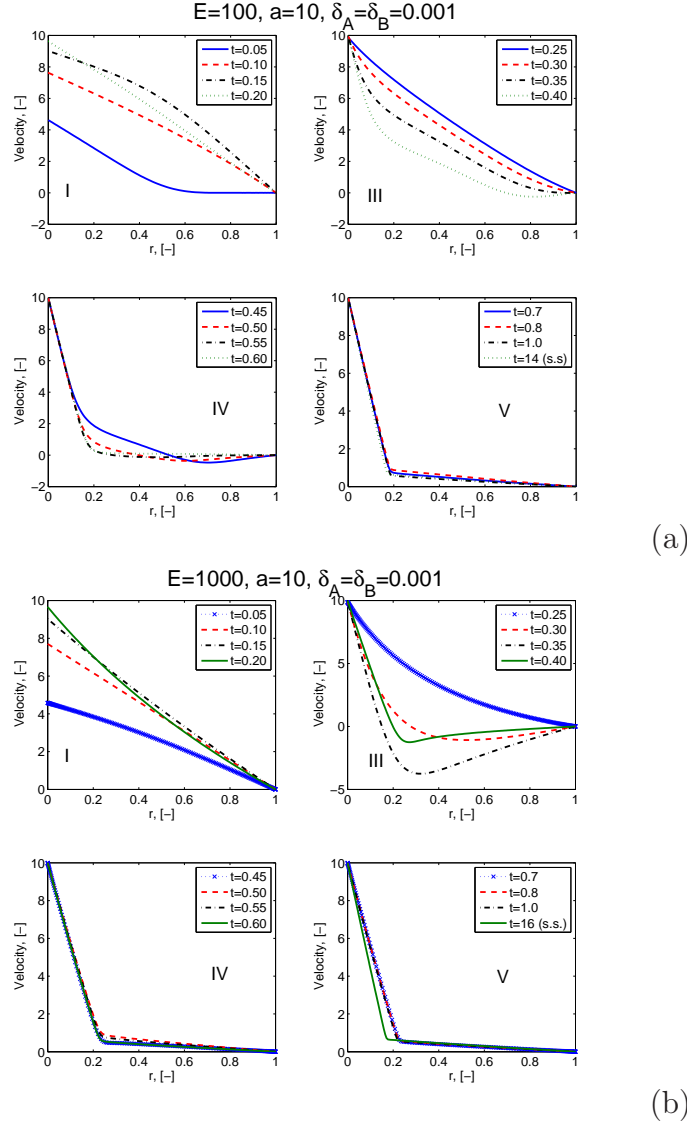
Fig. 13. Evolution in the velocity profiles across the gap during start up of a shear flow for a viscoelastic shear banding fluid; (a) larger inertia $E = 100$ and (b) smaller inertia $E = 1000$.

time response systematically we set $E \to \infty$ so that fluid inertial effects are excluded (as we have shown in Fig 12, inertia has no effect on the long-term behavior). In Fig. 14(b), we plot the time for the shear stress to reach steady state (denoted t_{ss}) as a function of the diffusion constant δ and the apparent shear rate De. In the range of $10^{-5} \leq \delta \leq 10^{-2}$ and for $De = 5, 10, 20$, the

38

computed time for the shear stress to reach steady state scales with $t_{ss} \sim \delta^{-1/2}$ as indicated by the solid line. This relationship breaks down for large values of $\delta > 10^{-2}$ because the diffusive layer is broader and there is interaction with the wall [42]. This observed scaling is consistent with experiments [38].
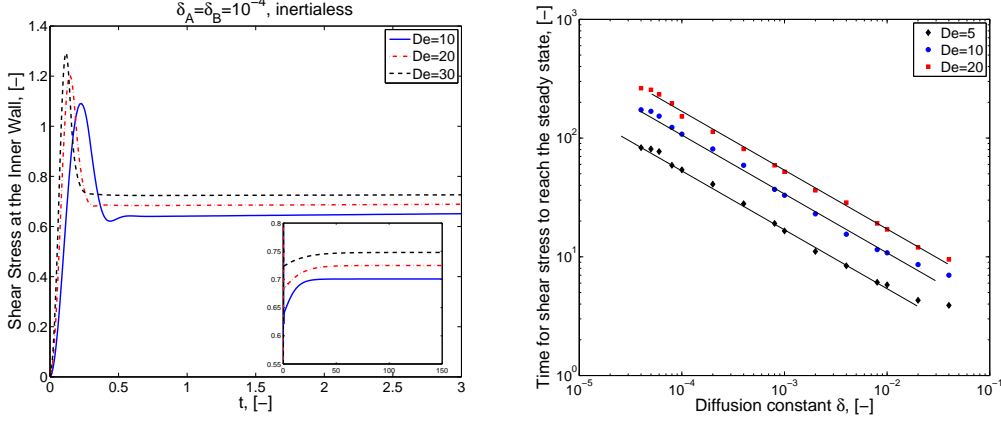

Fig. 14. (a) Responses of the shear stress for different apparent shear rates with a fixed value of the diffusion constant $\delta = 10^{-4}$. (b) Time for shear stress to reach steady state as a function of diffusion constant for selected $De = 5, 10, 20$. The straight lines show a scaling of $t_{ss} \sim \delta^{-1/2}$.

In [52], the dimensionless time to reach steady state is estimated to be

$$t_{ss} = \mu \frac{N}{\sqrt{\delta}} \frac{De}{\Delta\dot{\gamma}}, \tag{6}$$

where the apparent shear rate value is close to the left (low shear rate) end of the plateau, i.e. $De \sim \dot{\gamma}_M$. In this expression N is a dimensionless number determined by the model and $\Delta\dot{\gamma}$ is the dimensionless breadth of the plateau, $\Delta\dot{\gamma} = \dot{\gamma}_1 - \dot{\gamma}_2$. This result shows that the time for the shear stress to reach its final steady state is proportional to the apparent shear rate when the apparent shear rate $De = V'\lambda_{eff}/H$ is close to the critical value at which banding onsets. This general scaling also appears to be initially true in the

VCM model. In Fig. 14(b), when imposed apparent shear rate is increased from $De = 5$ to $De = 10$, the time t_{ss} to reach steady state doubled. However, when De increases further from 10 to 20, this is no longer true. Using this expression in Eqn. (6) and the data from Fig. 14 we determine values of $\mu N \sim 6$ for the VCM model, therefore $N \sim 1$. This value of N is approximate 3 times larger than estimates found from the diffusive Johnson-Segalman model [38, 52]. This expression enables us to obtain an estimation of the diffusion constant from experimental data in the start-up of steady shear flow. If t_{ss} is measured, then the dimensional diffusion constant D can be computed from the VCM model in the following way,

$$D = \left(\frac{N \, De}{\mu t_{ss} \Delta \dot{\gamma}} \right)^2 \cdot \frac{H^2}{\lambda_{eff}} \tag{7}$$

where, as indicated above the precise value of the numerical constant N varies for different fluid formulations and different models.

4   Conclusion

This paper, Part III of a sequence of papers, described respectively: the VCM model, new experimental findings relative to shear flow of a wormlike micellar solution, and the (inhomogeneous) predictions of the VCM model[7, 24]. The VCM model is a two species model proposed to study wormlike micelles with breakage and reforming events incorporated in a self-consistent way. In this paper, the third of the series, the spatio-temporal predictions of the VCM model in a Taylor-Couette shearing flow were presented. First, the model predictions for steady state flow were assembled namely the flow curve, the first normal stress difference as a function of apparent shear rate and the shear banded velocity profiles across the Couette cell gap. Then, a complete investigation of

the effect of varying the model parameters on the steady state flow curve was examined. It was shown that the parameter ξ which multiplies the nonlinear breakage term and thus determines the importance of the breakage can be scaled out of the shear flow governing equation if an inertialess simulation is considered.

The VCM model predictions were compared with a particular set of data from two mixed experiments (Taylor-Couette at low shear rates, microchannel at high shear rates) and reasonable agreement was shown. As noted in an earlier paper [29], experiments in a microchannel will only generate flow curves which agree directly with those of a Couette cell for particular choices of the driving pressure.

The effect of the start-up ramp rate and the role of geometry (curvature) on the steady state flow curve was examined, and the overshoot and undershoot observed in steady flow curve at the beginning and end of the plateau region was discussed. We also showed the hysteresis at the beginning of the flow curve plateau as well as the associated temporal evolution of the shear stress profiles. A complete description of the dynamics observed in the stress and velocity fields, from the initial formation of inertial waves (studied more carefully in [28]), through the time of the stress overshoot and shear band formation to the long time diffusion-mediated achievement of the steady state stress, was presented.

Most of the phenomena discussed have been documented in experimental work with micellar fluids. This class of model, a two species session-reforming model, thus appears to capture many of the key features that characterize micellar fluids whilst also being amenable to computational analysis.

5 Acknowledgements

References

[1] C. Grand, J. Arrault, and M.E. Cates. Slow transients and metastability in wormlike micelle rheology. *J. Phys. II France*, 7:1071–1086, 1997.

[2] J. B. Salmon, A. Colin, S. Manneville, and F. Molino. Velocity profiles in shear-banding wormlike micelles. *Phys. Rev. Lett.*, 90:228303–1 – 228303–4, 2003.

[3] L. Becu, S. Manneville, and A. Colin. Spatiotemporal dynamics of worm-like micelles under shear. *Phys. Rev. Lett.*, 93(1):018301–1–018301–4, 2004.

[4] Y.T. Hu and A. Lips. Kinetics and mechanism of shear banding in entangled micellar solutions. *J. Rheol.*, 49:1101–1027, 2005.

[5] J. F. Berret. Rheology of wormlike micelles : Equilibrium properties and shear banding transition. *Book Chapter in Molecular Gels; Eds. Springer: Dordrecht*, pages 235–275, 2005.

[6] E. Miller and J. P. Rothstein. Transient evolution of shear banding in wormlike micelle solutions. *J. Non-Newtonian Fluid Mech.*, 143:22–37, 2007.

[7] C.J. Pipe, N.J. Kim, P.A. Vasquez, L.P. Cook, and G.H. McKinley. Wormlike micellar solutions II: Comparison between experimental data and scission model predictions. *J. Rheol.*, 54:881–914, 2010.

[8] S. Lerouge and J-F. Berret. Shear-induced transitions and instabilities in surfactant wormlike micelles. *Adv. Polym. Sci*, 230:1–71, 2010.

[9] P. D. Olmsted. Perspectives on shear banding in complex fluids. *Rheol. Acta*, 47:283–300, 2008.

[10] M.E. Cates and S.M. Fielding. Rheology of giant micelles. *Advances in Physics*, 55:799–879, 2006.

[11] J. Yerushalmi, S. Katz, and R. Shinnar. The stability of steady shear flows of some viscoelastic fluids. *Chemical Eng. Sci.*, 25:1891–1902, 1970.

[12] S. M. Fielding. Complex dynamics of shear banded flows. *Soft Matter*, 2:1262–1279, 2007.

[13] S. M. Fielding and P. D. Olmsted. Early stage kinetics in a unified model of shear-induced demixing and mechanical shear banding instabilities. *Phys. Rev. Lett.*, 90:2240501–1 – 2240501–4, 2003.

[14] S. M. Fielding and P. D. Olmsted. Kinetics of shear banding instability in startup flows. *Phys. Rev. E*, 68:036313–1–036313–4, 2003.

[15] O. Radulescu and P. D. Olmsted. Matched asymptotic solutions for the steady banded flow of the diffusive Johnson-Segalman model in various geometries. *J. Non-Newtonian Fluid Mech.*, 91:143–164, 2000.

[16] M.E. Cates. Nonlinear viscoelasticity of wormlike micelles (and other reversibly breakable polymers). *J. Phys. Chem.*, 94:371–375, 1990.

[17] N.A. Spenley, X.F. Yuan, and M.E. Cates. Nonmonotonic constitutive laws and the formation of shear-banded flows. *J.Phys. II France*, 6:551–571, 1996.

[18] J. M. Adams, S. M. Fielding, and P. D. Olmsted. Transient shear banding in entangled polymers: A study using the Rolie-Poly model. *J. Rheol.*, 55(5):1007–1032, 2011.

[19] M. E. Helgeson, P. A. Vasquez, E. W. Kaler, and N. J. Wagner. Rheology and spatially resolved structure of cetyltrimethylammonium bromide wormlike micelles through the shear banding transition. *J. Rheol.*,

33:727–756, 2009.

[20] B. Yesilata, C. Clasen, and G.H. McKinley. Nonlinear shear and extensional flow dynamics of wormlike surfactant solutions. *J. Non-Newtonian Fluid Mech.*, 133:73–90, 2006.

[21] P. Fischer and H. Rehage. Non-linear flow properties of viscoelastic surfactant solutions. *Rheol. Acta*, 36:13–27, 1997.

[22] L. Zhou, P. A. Vasquez, L. P. Cook, and G. H. McKinley. Modeling the inhomogeneous response and formation of shear bands in steady and transient flows of entangled liquids. *J. Rheol.*, 52:591–623, 2008.

[23] R. G. Larson. *Constitutive Equations for Polymer Melts and Solutions.* Butterworths Series in Chemical Engineering, ed. H. Brenner. Butterworths, Boston, 1988.

[24] P. A. Vasquez, G. H. McKinley, and L. P. Cook. A network scission model for wormlike micellar solutions I: Model formulation and homogeneous flow predictions. *J. Non-Newtonian Fluid Mech.*, 144:122–139, 2007.

[25] R. L. Moorcroft and S. M. Fielding. Shear banding in time-dependent flows of polymers and wormlike micelles. *J. Rheol.*, 58:103–147, 2014.

[26] N. Germann, L.P. Cook, and A.N. Beris. Nonequilibrium thermodynamic modeling of the structure and rheology of concentrated wormlike micellar solutions. *J. Non-Newtonian Fluid Mech.*, 196:51–57, 2013.

[27] L. Zhou, L. P. Cook, and G. H. McKinley. Probing shear-banding transitions of the VCM model for entangled wormlike micellar solutions using large amplitude oscillatory shear (LAOS) deformations. *J. Non-Newt. Fluid Mech.*, 165:1462–1472, 2010.

[28] L. Zhou, L. P. Cook, and G. H. McKinley. Multiple shear-banding transitions for a model of wormlike micellar solutions. *SIAM J. Appl. Math.*, 72:1192–1212, 2012.

[29] M. Cromer, L.P. Cook, and G.H. McKinley. Pressure-driven flow of worm-like micellar solutions in rectilinear microchannels. *J. Non-Newt. Fluid Mech*, 166:180–193, 2011.

[30] M. Cromer, L.P. Cook, and G.H. McKinley. Extensional flow of wormlike micelles. *Chem. Eng. Sci.*, 64:4588–4596, 2009.

[31] N. Dubash, J. Cardiel, P. Cheung, and A. Q. Shen. A stable flow-induced structured phase in wormlike micellar solutions. *Soft Matter*, 7:876–879, 2011.

[32] Amy Q. Shen and Perry Cheung. The freedom of confinement in complex fluids. *Physics Today*, pages 30–35, September 2010.

[33] M. Vasudevan, E. Buse, D. Lu, H. Krishna, R. Kalyanaraman, A. Q. Shen, B. Khomami, and R. Sureshkumar. Irreversible nanogel formation in surfactant solutions by microporous flow. *Nat. Mat.*, 9:436–442, 2010.

[34] Official symbols and nomenclature of the society of rheology. *J. Rheol.*, 57:1047–1055, 2013.

[35] K. E. Brenan, S. L. Campbell, and L. R. Petzold. *Numerical Solution of Initial-Value Problems in Differential-Algebraic Equations*. SIAM Classics in Applied Mathematics, Philadelphia, first edition, 1996.

[36] T. W. Tee and L. N. Trefethen. A rational spectral collocation method with adaptively transformed chebyshev grid points. *SIAM J. Sci. Comp*, pages 1798–1811, 2005.

[37] M.R. Lopez-Gonzales, W.M. Holmes, and P.T. Callaghan. Rheo-NMR phenomena of wormlike micelles. *Soft Matter*, 2:855–869, 2006.

[38] S. Lerouge, M.A. Fardin, M. Argentina, G. Grégoire, and O. Cardoso. Interface dynamics in shear-banding flow of giant micelles. *Soft Matter*, 4:1808–1819, 2008.

[39] P.D. Olmsted, O. Radulescu, and C.-Y.D. Lu. Johnson-Segalman model

with a diffusion term in cylindrical Couette flow. *J. Rheol.*, 44:257–275, 2000.

[40] M. A. Fardin and S. Lerouge. Instabilities in wormlike micelle systems. *Eur. Phys. J. E*, 35:12091, 2012.

[41] S. M. Fielding. Viscoelastic Taylor-Couette instability of shear banded flow. *Phys. Rev. Lett.*, 104:198303, 2010.

[42] O. Radulescu, P. D. Olmsted, and C.-Y.D. Lu. Shear banding in reaction-diffusion models. *Rheol. Acta*, 38:606–613, 1999.

[43] M. A. Farding, T.J. Ober, C. Gay, G. Gregoire, G. H. McKinley, and S. Lerouge. Potential "ways of thinking" about the shear-banding phenomenon. *Soft Matter*, 8:910–922, 2012.

[44] C. J. Pipe, T. S. Majmudar, and G. H. McKinley. High shear rate viscometry. *Rheol Acta*, 47:621–642, 2008.

[45] C. Masselon, J-B. Salmon, and A. Colin. Nonlocal effects in flows of wormlike micellar solutions. *Phys. Rev. Lett.*, 100:038301, 2008.

[46] P. Nghe, S. M. Fielding, P. Tabeling, and A. Ajdari. Interfacially driven instability in the microchannel flow of a shear-banding fluid. *Phys. Rev. Lett.*, 104:248303, 2010.

[47] L. Casanellas and G. H. McKinley. *Private communication.*

[48] M. Cromer. *Private communication.*

[49] S. Kumar and R.G. Larson. Shear banding and secondary flow in viscoelastic fluids between a cone and plate. *J. Non-Newtonian Fluid Mech.*, 95:295–314, 2000.

[50] A.F. Méndez-Sánchez, M.R. López-González, V.H. Rolón-Garrido, J. Pérez-González, and L. de Vargas. Instabilities of micellar systems under homogeneous and non-homogeneous flow conditions. *Rheol. Acta*, 42:56–63, 2003.

[51] S. Manneville, J.B. Salmon, L. Becu, A. Colin, and F. Molino. Inhomogeneous flows in sheared complex fluids. *Rheol. Acta.*, 43:408–416, 2004.

[52] O. Radulescu, P. D. Olmsted, J. P. Decruppe, S. Lerouge, J. F. Berret, and G. Porte. Timescales in shear banding of wormlike micelles. *Europhys. Lett.*, 62(2):230–236, 2003.